Viscosity Control of the Dynamic Self-Assembly in Ferromagnetic Suspensions

D. L. Piet,[1,2] A. V. Straube,[3,2] A. Snezhko,[2] and I. S. Aranson[2,1]

[1]*Department of Engineering Science and Applied Mathematics, Northwestern University, 2145 Sheridan Road, Evanston, Illinois 60208, USA*

[2]*Materials Science Division, Argonne National Laboratory, 9700 South Cass Avenue, Argonne, Illinois 60439, USA*

[3]*Department of Physics, Humboldt University of Berlin, Newtonstraße 15, 12489 Berlin, Germany*

(Received 14 December 2012; published 7 May 2013)

Recent studies of dynamic self-assembly in ferromagnetic colloids suspended in liquid-air or liquid-liquid interfaces revealed a rich variety of dynamic structures ranging from linear snakes to axisymmetric asters, which exhibit novel morphology of the magnetic ordering accompanied by large-scale hydrodynamic flows. Based on controlled experiments and first principles theory, we argue that the transition from snakes to asters is governed by the viscosity of the suspending liquid where less viscous liquids favor snakes and more viscous, asters. By obtaining analytic solutions of the time-averaged Navier-Stokes equations, we gain insight into the role of mean hydrodynamic flows and an overall balance of forces governing the self-assembly. Our results illustrate that the viscosity can be used to control the outcome of the dynamic self-assembly in magnetic colloidal suspensions.

DOI: 10.1103/PhysRevLett.110.198001 PACS numbers: 82.70.Dd, 45.70.−n, 75.50.Tt, 81.16.Dn

Fundamental principles guiding self-assembly in nonequilibrium colloidal systems continue to attract enormous attention in physics and engineering communities [1–13]. The interest is stimulated by the need for creating smart materials capable of self-assembly, adaptation, and for the design of tunable structures that can perform useful tasks at the microscale [14], including targeted cargo delivery [15], stirring in microfluidic devices [16], and control of optical properties of the media [17].

Studies of dynamic self-assembly in ferromagnetic colloids dispersed at liquid-air interfaces [18,19] and energized by an alternating (ac) magnetic field revealed highly organized, dynamic linear structures—magnetic snakes. The snake emerges spontaneously from a random dispersion of particles in a certain range of frequencies and amplitudes of the ac magnetic field. While for low frequencies of the applied magnetic field the snakes are immobile, with the increase in frequency they turn into self-propelled entities [20]. Surprisingly, fundamentally new structures—localized magnetic asters and arrays of asters—emerge when the same colloidal suspension is confined at the interface between two immiscible liquids and is energized by the alternating magnetic field [21].

Both magnetic snakes and asters generate complex flows in the fluid and possess magnetic ordering and dynamic organization highly unfavorable under equilibrium conditions. While magnetic snakes are essentially linear and composed of antiferromagnetically ordered segments of ferromagnetically ordered chains of microparticles [18], asters develop radial structural order with the ferromagnetically ordered chains emanating from the center of each aster [21]. The mean flows excited by the snakes and asters have fundamentally different morphology: snakes create quasi-two-dimensional flows with quadrupole symmetry confined near the surface [19] and asters induce three-dimensional toroidal bulk flows [21]. The main forces that control dynamic self-assembly in such systems involve not only magnetic dipole-dipole and steric interactions between the particles but also nontrivial hydrodynamic forces stemming from deformation of the interface, viscous drag, and entrainment by the large-scale mean flow. The striking difference between self-assembled structures in liquid-air and liquid-liquid systems remained unclear since both systems were driven similarly. Thus, it is critical to understand the fundamental physical parameters controlling the transition between these two distinctive dynamic states.

In this Letter, we perform a systematic experimental and theoretical study of the snake-aster transition. It is widely believed that, because the motion of each individual colloidal particle is strongly overdamped, the viscosity sets only an overall time scale. Moreover, the motion of fluid is often described by the linear Stokes equation, as, e.g., in Ref. [22], and admits a one-way coupling between the solvent and the particles, when only the particle dynamics is influenced by the liquid flow but not vice versa [23]. For our system, neither of these assumptions is met, presenting a great challenge for the theory. However, on the basis of controlled experiments and comprehensive analysis of the first principles model, we have demonstrated that the viscosity defines the intricate balance between magnetic forces and hydrodynamic forces arising from the inertia of the particles and suspending liquid. The magnitude of these forces is inversely proportional to the viscosity, which can be independently controlled both in our experiment and in the theoretical model. We show that at a given frequency and amplitude of the energizing ac magnetic field the viscosity of a suspending liquid controls the transition between

snakes and asters; snakes emerge for smaller viscosities, while asters are favored in more viscous liquids.

In our experiments with liquid-air systems, the structural transition from snakes to asters is consistently observed when the viscosity of suspending liquid is gradually increased. Our theoretical model, the fully nonlinear Navier-Stokes equations coupled to the dynamics of individual magnetic particles, is reduced to a set of closed, time-averaged ordinary differential equations for particle positions and orientations interacting via magnetic forces and effective mean hydrodynamic forces arising due to oscillation of massive particles in a viscous liquid. The cause of these mean forces is Stokes drift and Rayleigh streaming. In contrast to the earlier study based on direct simulation of the Navier-Stokes equations [24], here we obtain their analytic solutions, which provide deep insight into the role of hydrodynamic flows, their detailed structure, and an overall balance of forces governing the self-assembly. The model is in good qualitative (and some times quantitative) agreement with the experiments.

Our experimental apparatus was similar to that described in Ref. [18]. A ferromagnetic colloidal suspension was composed of nickel microspheres with an average size of 90 μm (Alfa Aesar Company). Because of defects in particles, their magnetic moments are often strongly pinned and the particles behave as magnetically "hard" microspheres. The particles were dispersed at the liquid-air interface, where they were supported by a surface tension. To exclude the difference between the deep and shallow liquid layers, a circular glass beaker (5 cm in diameter) was filled with liquid depths of 5 cm and 5 mm.

To vary the viscosity of the liquid, a range of water-sucrose solutions was prepared [25]. The colloidal suspension was energized by an ac magnetic field, $H_{\rm ac} = H_0 \sin(2\pi f t)$, with the frequency f and amplitude $H_0 = 200$ Oe, applied perpendicular to the interface.

Selected experimental results are summarized in Fig. 1. We observed the formation of magnetic snakes for values of the dynamic viscosity of the suspending liquid η close to the viscosity of water, $\eta \approx 1$ mPa s. With a gradual increase in η, the snakes give way to asters, as illustrated in Fig. 1, top panel. The transition is not sharp, it is associated with a wide transition region, as indicated by the error bars. Remarkably, the transition line is almost parallel to the η axis above the viscosity of $\eta \approx 12$ mPas. The bottom panel of Fig. 1 shows a characteristic time T_f for the formation of snake or aster as a function of η for $f = 40$ Hz. After this time, the size of the developed structure almost did not change; the change of its relative size was within 10%. Despite relatively large error bars, T_f gradually increases with the growth of η.

To obtain insights into the snake-aster transition, we significantly extend our model developed in Ref. [24]. We start with the model based on the fully nonlinear Navier-Stokes equation in the shallow water approximation,

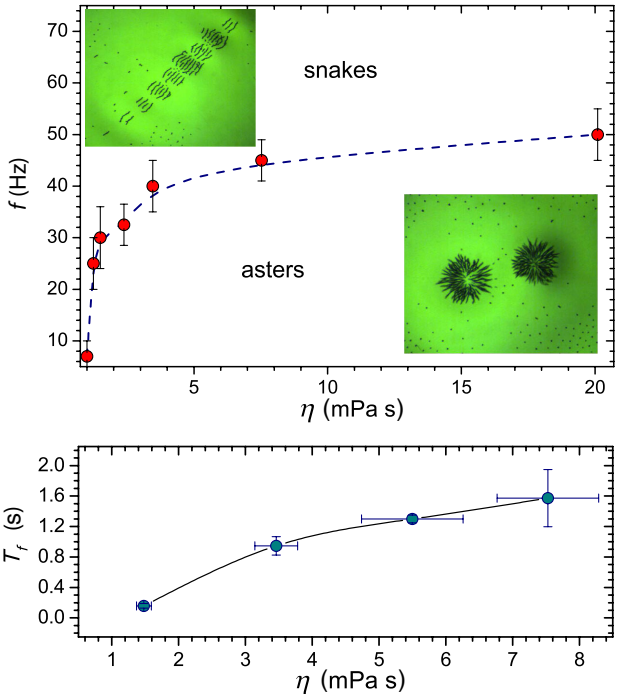

FIG. 1 (color online). Top panel: Snake-aster phase diagram as a function of frequency f and viscosity η. The amplitude of the ac magnetic field is $H_0 = 200$ Oe. Insets: Representative images of a snake (top) and an aster (bottom). Bottom panel: Characteristic time T_f for the formation of snakes (or asters) as a function η for $f = 40$ Hz and $H_0 = 200$ Oe. For two points the vertical error bars are smaller than the markers.

$$\partial_t h + \nabla \cdot (h\mathbf{v}) = 0, \tag{1}$$

$$\partial_t \mathbf{v} + (\mathbf{v}\cdot\nabla)\mathbf{v} = \nu(\nabla^2\mathbf{v} - \alpha\mathbf{v}) - \nabla h + \gamma\nabla\nabla^2 h + H_0 \sin(\omega t)\sum_i s(\mathbf{r} - \mathbf{r}_i)\mathbf{P}_i, \tag{2}$$

where $\mathbf{v}$ is the two-dimensional (2D), in-plane fluid velocity, h is the surface elevation, ν is the kinematic viscosity, α is the friction with the bottom of the container, and γ is the surface tension. The last term in Eq. (2) is representative of forces applied to the surface of the fluid through the particles, where H_0 is the amplitude of the ac magnetic field, ω is the frequency, the localized function s defines the shape of the particle, and $\mathbf{P}_i \equiv (\cos\phi_i, \sin\phi_i)$ is the orientation of the dipole moment of the ith particle. In our study, we neglect the surface tension [26] and assume that s is given by delta functions $\delta(\mathbf{r} - \mathbf{r}_i)$, which does not affect the basic physics of self-assembly but, more importantly, makes our model analytically tractable. The variables are scaled as follows: coordinates $\mathbf{r} \to \mathbf{r}/h_0$, time $t \to t\sqrt{h_0/g}$, velocity $\mathbf{v} \to \mathbf{v}/\sqrt{gh_0}$, viscosity $\nu \to \nu/h_0\sqrt{gh_0}$, where g is gravitational acceleration. In this dimensionless, rescaled equation, $\alpha = h_0 = 1$.

The motion of the particles on the surface of the fluid is described using Newton's equations

$$m\ddot{\mathbf{r}}_i + \mu_t\dot{\mathbf{r}}_i = \mathbf{F}_i + \mu_t\mathbf{v} - \beta\nabla h, \quad (3)$$

$$I\ddot{\boldsymbol{\phi}}_i + \mu_r\dot{\boldsymbol{\phi}}_i = \mathbf{T}_i + \kappa H_0 \sin(\omega t)\nabla h \times \mathbf{P}_i, \quad (4)$$

where m, I, μ_t, μ_r are the particle mass, moment of inertia, and translational and rotational friction coefficients, respectively; $\beta = mg$, $\mathbf{F}_i = \sum_{j\neq i}\mathbf{F}_{ij}$, and $\mathbf{T}_i = \sum_{j\neq i}\mathbf{T}_{ij}$ are, respectively, the forces and torques on particle i due to magnetic and steric interactions with all other particles, $\mu_t\mathbf{v}$ is the Stokes' drag, and $-\beta\nabla h$ is the movement along the surface gradient from gravity. The last term in Eq. (4) is the torque applied to each dipole moment in the direction of the projection of the vertical ac field on deformed surface [24].

In previous work, Eqs. (1)–(4) were solved numerically to model snakes [24]. Here, we first analytically find solutions of Eqs. (1) and (2) in an asymptotic limit where we expand the surface deformation and liquid velocity with respect to the small parameter ϵ, $h = h_0 + \epsilon h_1 + \epsilon^2 h_2 + \mathcal{O}(\epsilon^3)$ and $\mathbf{v} = \epsilon\mathbf{v}_1 + \epsilon^2\mathbf{v}_2 + \mathcal{O}(\epsilon^3)$. The parameter ϵ can be interpreted as the relative deviation of the locus $h(\mathbf{r}, t)$ of the liquid-air interface from the equilibrium value h_0. Moreover, by using the dimensionless viscosity ν as a small parameter, Eqs. (1) and (2) were analytically solved up through the first order for the corresponding surface deformation and 2D velocity fields induced by each particle individually to yield $h_1(\mathbf{r}, t) = h_r(\mathbf{r})e^{i\omega t} + \text{c.c.}$ and $\mathbf{v}_1(\mathbf{r}, t) = \mathbf{v}_r(\mathbf{r})e^{i\omega t} + \text{c.c.}$, where c.c. denotes the complex conjugate. At the second order, time-averaged solutions h_2 and $\mathbf{v}_2$ were sought and a corresponding analytic expression for $\mathbf{v}_2$, which determines the mean flow, was obtained [27,28].

Using the explicit solutions h_1, h_2, $\mathbf{v}_1$, and $\mathbf{v}_2$ of the nonlinear Navier-Stokes equations (1) and (2), we perform the time averaging of Eqs. (3) and (4). As a result, we arrive at a closed system of ordinary differential equations for the particles in which all of the details of the complex hydrodynamic flows are effectively encapsulated in pairwise interactions:

$$m\ddot{\mathbf{r}}_i + \mu_t\dot{\mathbf{r}}_i = \sum_{j\neq i}[\mathbf{F}_{ij} + \mathbf{s}_j + \mu_t\mathbf{v}_2^{(j)} - \beta\nabla h_2^{(j)}], \quad (5)$$

$$I\ddot{\boldsymbol{\phi}}_i + \mu_r\dot{\boldsymbol{\phi}}_i = \sum_{j\neq i}\left[\mathbf{T}_{ij} + \text{Im}\left\{\frac{\kappa H_0}{2}\nabla(h_r^{(j)} - \bar{h}_r^{(j)}) \times \mathbf{P}_i\right\}\right]. \quad (6)$$

Here, the overline denotes complex conjugate and $\mathbf{s}_j = -2m[\beta\nabla|\nabla h_r^{(j)}|^2 + \mu_t\{(\mathbf{v}_r^{(j)}\cdot\nabla)\bar{\mathbf{v}}_r^{(j)} + \text{c.c.}\}]/(\alpha^2 + m^2\omega^2)$ is the Stokes drift term. To obtain the Stokes drift of each particle, we treated each term on the right-hand side of Eq. (3) independently. The last term in Eq. (5) is of much smaller order and can be neglected.

Thus, in contrast to the earlier model [24], where the dynamics of the particles is determined by Eqs. (3) and (4) coupled to nonlinear equations (1) and (2), we suggest a much simpler and more transparent model in which the particle positions and orientations are described by Eqs. (5) and (6). Based on this model, we performed simulations with different numbers of particles ranging from 225 to 1000 [29], with an initial configuration on a perturbed square lattice with a uniformly random orientation of the dipole moment and run on a graphic processing unit cluster. In addition to a significant reduction of computation time, roughly an order of magnitude speed up, the great advantage of our approach is gaining insight into the surface flows as the central ingredient underlying self-assembly.

The overall analytic behavior of the mean surface flows, shown in Fig. 2, is similar to the large-scale quadrupolar flow seen from experiment. These flows are analogous to the mean flow produced by Rayleigh streaming [30]. The first-order flows ($\mathbf{v}_1$) are time dependent, dipolar flows that oscillate in space and decay out exponentially, $\mathbf{v}_r(\mathbf{r}) \propto \exp(-ikr)/\sqrt{r}$, with $k \approx \omega - i\nu k_1$, $k_1 = (\omega^2 + \alpha)/2$; the behavior of $h_r(\mathbf{r})$ with r is similar to that of $\mathbf{v}_r(\mathbf{r})$; see Fig. 2(d). The second-order mean flow $\mathbf{v}_2$ is time independent and is decomposed into the potential and rotational components, as shown in Figs. 2(a) and 2(b), respectively. Both these counterparts have a long-ranged quadrupolar structure with a monotonic power-law decay $\propto r^{-3}$. The full mean flow is seen in Fig. 2(c).

Note that since the localized shape function was modeled by the delta function, the velocities and surface

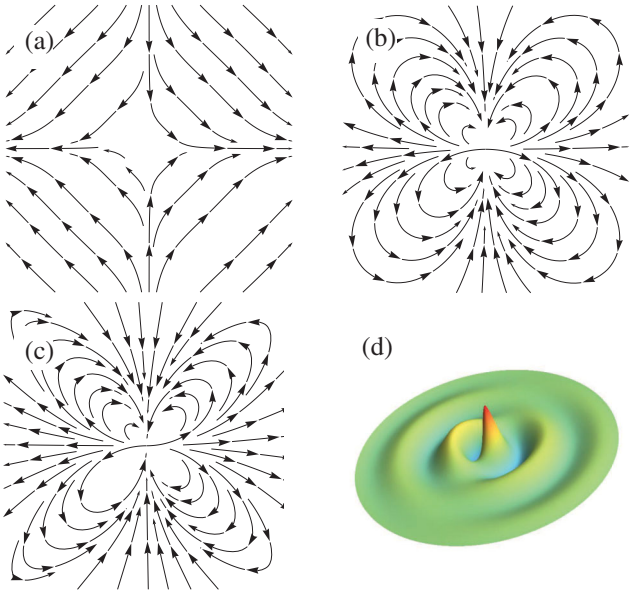

FIG. 2 (color online). Mean surface flows ($\mathbf{v}_2$) and first-order surface deformation (h_r) induced by a single particle. (a), (b) Quadrupole streamlines produced by the potential (a) and rotational (b) components of the mean flow $\mathbf{v}_2$. The magnitude of the velocity $\mathbf{v}_2$ decays as r^{-3}. (c) Composite of the potential and rotational flows. (d) First-order surface deformation h_r, which decays exponentially with r. The color in the image indicates the height.

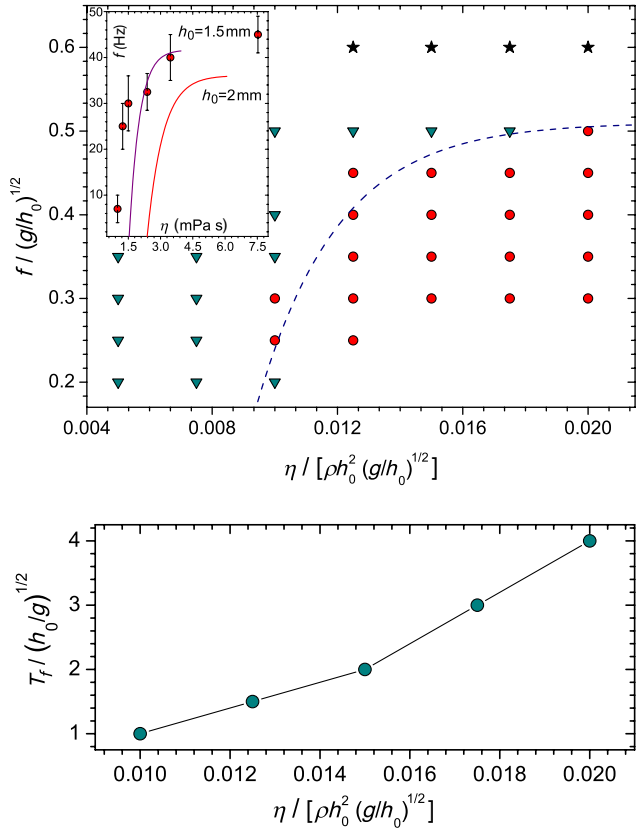

FIG. 3 (color online). Top panel: Snake-aster phase diagram as a function of the rescaled frequency and viscosity. Circles, triangles, and stars are, respectively, for asters, snakes, and a mixture of segments forming neither asters nor snakes. Inset: Comparison of experimental data (circles) and prediction of the model (solid lines) for $h_0 = 1.5$ mm and $h_0 = 2$ mm. Bottom panel: Formation time T_f of a structure as a function of fluid viscosity for $f(g/h_0)^{-1/2} = 0.3$.

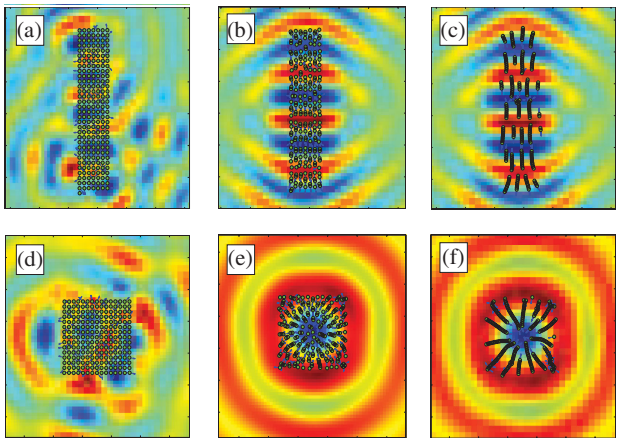

FIG. 4 (color online). Top row: Snake formation. (a) Particles on a rectangular lattice with random orientation. (b) Magnetic moments align along the surface gradient. Colors represent surface elevation h (red and blue show maxima and minima, respectively), arrows indicate particle magnetic moments. (c) Ferromagnetic chains are formed and are antiferromagnetically aligned, creating a snake. Bottom row: Formation of an aster. (d) Particles on a square lattice with random orientations. (e) Magnetic moments align along the surface gradient. (f) Ferromagnetically ordered chains are formed and an aster is assembled.

deformations at all orders diverge at the center of each particle. These divergences, however, have no effect on the system because each particle cannot influence itself, and for each pair of particles, a short-range steric repulsion prevents them from getting close enough to feel the divergence. Earlier experimental data [19] showed that a mean quadrupole flow was an essential ingredient for the assembly of snakes. Our model elucidates why this finding is true for both snakes and asters: neither of these structures can be reproduced in simulations via Eqs. (5) and (6) unless the Stokes drift and the mean flow (i.e., the fields h_r, $\mathbf{v}_r$, and $\mathbf{v}_2$) are properly determined.

A critical test of the model is to recover the crossover in the behavior from snakes to asters that was seen experimentally as a function of the liquid viscosity η and the field frequency f. The model successfully does so for a range of values of η and f, see Fig. 3, top panel, where $\alpha = h_0 = \rho = 1$. In qualitative agreement with the experiment, we observed snakes and asters formed for lower and higher values of η, respectively. Moreover, the dependence of time T_f for the formation of a dynamic structure on η exhibits a trend similar to the experimental one; see Fig. 3, bottom panel. Note that, in order to avoid depth dependence, the axes in Fig. 3 remain in dimensionless quantities. In the case where the viscosity was low and the frequency was high, the simulations yielded a clumping of particles primarily due to the lack of friction in the system. Alternately, when the viscosity was high and the frequency was low, the particles remained scattered due to overdamping and a lack of alignment along the changes in the surface height gradient.

Because the mean flow induced by each particle has a long-range nature, it affects the dynamics of all other particles, leading to a highly nontrivial self-organization of the system. Figure 4 illustrates the formation of snakes and asters from an initially disordered distribution of particles. The particles were dispersed uniformly inside a rectangle (snakes) or square (asters) with their magnetic moments oriented randomly. As Fig. 4 shows, asters and snakes are formed after a short transient (T_f), their organization, e.g., antiferromagnetic order, closely resembles the experimental one. Starting from different initial conditions, e.g., square for the case of snake, often resulted in the formation of more than one snake or aster.

In conclusion, we have demonstrated that the viscosity of the suspending liquid strongly affects the outcome of dynamic self-assembly and controls the structural transition between self-assembled structures. Linear snakes are favored for small viscosities and circular asters for higher viscosities. Our novel model provides a nontrivial insight

into how the large-scale mean flow—a nonlinear effect caused by the strong coupling of oscillating particles with the initially equilibrium liquid—becomes a critical player that not only determines the shape and organization of the emergent dynamic structures but also keeps them stable. As we show, both inertia of the liquid and inertia of the particles are at the heart of the assembly process.

While we were able to reproduce the main observed phenomenology, our method also has limitations. One shortfall is that, being a completely two-dimensional model, the shallow water equations do not capture the liquid jets into the bulk produced by asters [21]. However, our model is capable of replicating the overall structure of both snakes and asters. As snakes produce a largely 2D flow, it was natural to expect that they can be recovered from this model. Asters, however, produce a three-dimensional toroidal flow and their appearance in this model was not expected. They form due to the propensity of the dipoles to align along the surface gradient for large characteristic wavelengths, whereas entrainment by the large-scale toroidal flow is important but less critical. Another reason for the lack of a good quantitative agreement between the experiment and model (such as in the inset of Fig. 3, top panel) is due to the neglected surface tension. Along with gravity, it presents another mechanism for surface wave generation but makes the model analytically intractable.

This research was supported by the U.S. DOE, Office of Basic Energy Sciences, Division of Materials Science and Engineering, under Contract No. DE AC02-06CH11357. A. V. S. thanks Argonne's Materials Theory Institute for support of his visit to Argonne.

[1] G. Whitesides and B. Grzybowski, Science **295**, 2418 (2002).
[2] A. Snezhko, J. Phys. Condens. Matter **23**, 153101 (2011).
[3] J. E. Martin, Phys. Rev. E **79**, 011503 (2009); K. J. Solis and J. E. Martin, J. Appl. Phys. **111**, 073507 (2012).
[4] S. C. Glotzer and M. J. Solomon, Nat. Mater. **6**, 557 (2007).
[5] I. S. Aranson and L. S. Tsimring, Rev. Mod. Phys. **78**, 641 (2006); *Granular Patterns* (Oxford University Press, Oxford, England, 2009).
[6] P. Tierno, T. M. Fischer, T. H. Johansen, and F. Sagués, Phys. Rev. Lett. **100**, 148304 (2008).
[7] N. Osterman, I. Poberaj, J. Dobnikar, D. Frenkel, P. Ziherl, and D. Babić, Phys. Rev. Lett. **103**, 228301 (2009); M. Oettel and S. Dietrich, Langmuir **24**, 1425 (2008).
[8] M. E. Leunissen, H. R. Vutukuri, and A. van Blaaderen, Adv. Mater. **21**, 3116 (2009).
[9] N. Aubry, P. Singh, M. Janjua, and S. Nudurupati, Proc. Natl. Acad. Sci. U.S.A. **105**, 3711 (2008).
[10] G. Vernizzi and M. Olvera de la Cruz, Proc. Natl. Acad. Sci. U.S.A. **104**, 18382 (2007).
[11] M. V. Sapozhnikov, Y. V. Tolmachev, I. S. Aranson, and W.-K. Kwok, Phys. Rev. Lett. **90**, 114301 (2003).
[12] J. Yan, M. Bloom, S. C. Bae, E. Luijten, and S. Granick, Nature (London) **491**, 578 (2012).
[13] J. Dobnikar, A. Snezhko, and A. Yethiraj, Soft Matter **9**, 3693 (2013).
[14] B. A. Grzybowski, M. Radkowski, C. J. Campbell, J. N. Lee, and G. M. Whitesides, Appl. Phys. Lett. **84**, 1798 (2004).
[15] J. Edd *et al.*, in *Proceedings of the IEEE RSJ International Conference on Intelligent Robots and Systems* (IEEE, New York, 2003), Vol. 3, p. 2583.
[16] S. T. Chang, V. N. Paunov, D. N. Petsev, and O. D. Velev, Nat. Mater. **6**, 235 (2007).
[17] S. K. Y. Tang, R. Derda, A. D. Mazzeo, and G. M. Whitesides, Adv. Mater. **23**, 2413 (2011).
[18] A. Snezhko, I. S. Aranson, and W.-K. Kwok, Phys. Rev. Lett. **96**, 078701 (2006); Phys. Rev. E **73**, 041306 (2006).
[19] M. Belkin, A. Snezhko, I. S. Aranson, and W.-K. Kwok, Phys. Rev. Lett. **99**, 158301 (2007).
[20] A. Snezhko, M. Belkin, I. S. Aranson, and W.-K. Kwok, Phys. Rev. Lett. **102**, 118103 (2009).
[21] A. Snezhko and I. S. Aranson, Nat. Mater. **10**, 698 (2011).
[22] S. Martens, A. V. Straube, G. Schmid, L. Schimansky-Geier, and P. Hänggi, Phys. Rev. Lett. **110**, 010601 (2013).
[23] A. V. Straube, J. Phys. Condens. Matter **23**, 184122 (2011).
[24] M. Belkin, A. Glatz, A. Snezhko, and I. S. Aranson, Phys. Rev. E **82**, 015301 (2010).
[25] M. Migliori, D. Gabriele, R. Di Sanzo, B. de Cindio, and S. Correra, J. Chem. Eng. Data **52**, 1347 (2007).
[26] While lateral capillary forces can influence the outcome of colloidal assembly, see, e.g., R. Di Leonardo, F. Saglimbeni, and G. Ruocco, Phys. Rev. Lett. **100**, 106103 (2008), in our case capillary interactions (of the order of pN) are negligible compared to magnetic and hydrodynamic forces (of the order of nN).
[27] L. D. Landau and E. M. Lifshitz, *Fluid Mechanics* (Pergamon, Oxford, 1987), 2nd ed.
[28] A. H. Nayfeh, *Introduction to Perturbation Techniques* (Wiley, New York, 1981).
[29] A. Hucht, S. Buschmann, and P. Entel, Europhys. Lett. **77**, 57003 (2007).
[30] N. Riley, Theor. Comput. Fluid Dyn. **10**, 349 (1998).